Submitted to The Astrophysical Journal

Bar Diagnostics in Edge-On Spiral Galaxies. III. N-Body Simulations of Disks

M. Bureau[1,2]

Columbia Astrophysics Laboratory, 550 West 120th Street, 1027 Pupin Hall, MC 5247, New York, NY 10027

bureau@astro.columbia.edu

and

E. Athanassoula

Observatoire de Marseille, 2 place Le Verrier, F-13248 Marseille Cedex 4, France

ABSTRACT

Present in over 45% of local spirals, boxy and peanut-shaped bulges are generally interpreted as edge-on bars and may represent a key phase in bar evolution. Aiming to test such claims, the kinematic properties of self-consistent 3D N-body simulations of bar-unstable disks are studied. Using Gauss-Hermite polynomials to describe the major-axis stellar kinematics, a number of characteristic bar signatures are identified in edge-on disks: 1) a major-axis light profile with a quasi-exponential central peak and a plateau at moderate radii (Freeman Type II profile); 2) a "double-hump" rotation curve; 3) a sometime flat central velocity dispersion peak with a plateau at moderate radii and occasional local central minimum and secondary peak; 4) an $h_3 - V$ correlation over the projected bar length. All those kinematic features are spatially correlated and can easily be understood from the orbital structure of barred disks. They thus provide a reliable and easy-to-use tool to identify edge-on bars. Interestingly, they are all produced without dissipation and are increasingly realized to be common in spirals, lending

[1]Hubble Fellow

[2]Now at Sub-Department of Astrophysics, University of Oxford, Denys Wilkinson Building, Keble Road, Oxford OX1 3RH, United Kingdom

support to bar-driven evolution scenarios for bulge formation. So called "figure-of-eight" position-velocity diagrams are never observed, as expected for realistic orbital configurations. Although not uniquely related to triaxiality, line-of-sight velocity distributions with a high velocity tail (i.e. an $h_3 - V$ correlation) appear as particularly promising tracers of bars. The stellar kinematic features identified grow in strength as the bar evolves and vary little for small inclination variations. Many can be used to trace the bar length. Comparisons with observations are encouraging and support the view that boxy and peanut-shaped bulges are simply thick bars viewed edge-on.

Subject headings: celestial mechanics, stellar dynamics — galaxies: kinematics and dynamics — galaxies: bulges — galaxies: spiral — galaxies: structure — instabilities

1. Introduction

Three-dimensional (3D) N-body simulations of bar-unstable disks have consistently shown that, soon after a bar forms, it buckles and settles with an increased thickness and velocity dispersion, appearing boxy or peanut-shaped (B/PS) when viewed edge-on (e.g. Combes & Sanders 1981; Combes et al. 1990; Raha et al. 1991). This is particularly important in view of the large number of vertically extended structures commonly refered to as B/PS bulges in edge-on spirals. The recent survey of Lütticke, Dettmar, & Pohlen (2000a) reveals that at least 45% of bulges across all morphological types are B/PS (but see also the earlier studies of Jarvis 1986; de Souza & dos Anjos 1987; Shaw 1987), suggesting that a significant fraction of bulges may form through dynamical instabilities in disks rather than dissipational collapse (e.g. Eggen, Lynden-Bell, & Sandage 1962) or accretion of smaller systems (e.g. Searle & Zinn 1978).

Verifying such claims is hard, as reliably identifying bars in edge-on systems is difficult. A plateau in the major-axis light profile of an edge-on spiral has long been claimed to indicate the presence of a bar (e.g. de Carvalho & da Costa 1987; Hamabe & Wakamatsu 1989; Lütticke, Dettmar, & Pohlen 2000b), but axisymmetric features could equally give rise to it and end-on bars would likely remain undetected. A kinematic identification is clearly called for, analogous to the use of longitude-velocity diagrams in the Galaxy (Peters 1975; Mulder & Liem 1986; Binney et al. 1991; etc). This was first proposed and used in the context of external bulges by Kuijken & Merrifield (1995), while Bureau & Athanassoula (1999, hereafter Paper I) and Athanassoula & Bureau (1999, hereafter Paper II) refined those kinematic bar diagnostics using, respectively, periodic orbit calculations and hydrodynamical

simulations. These were then applied to relatively large samples of galaxies by Merrifield & Kuijken (1999) and Bureau & Freeman (1999), who successfully showed a close relationship between B/PS structures and bars. Using the ionized-gas kinematics, these works were however only able to probe the galactic potentials in the equatorial plane and were restricted to intermediate and late-type spirals.

Using N-body simulations, we develop in this paper fully self-consistent stellar kinematic bar diagnostics for edge-on systems. Those diagnostics are most easily applicable to gas-poor early-type spirals (where the bulges are large and contain little dust, perfect for photometric studies), and they allow to probe galactic potentials out of the disk plane (to test the barred nature of B/PS structures at large galactic heights). The diagnostics rely exclusively on readily observable quantities and are thus not meant as a study of barred N-body models. They have already been successfully applied by Chung & Bureau (2004) to the complete sample of Bureau & Freeman (1999), and they are being applied at different heights to a subset of the galaxies by Zamojski et al. (2005, in preparation). Bureau et al. (2005) and Athanassoula, Aronica, & Bureau (2005) present K-band observations of the same sample, quantifying the B/PS structure. The goal of all those studies is to study the vertical structure of bars, and ultimately to clarify their relationship to bulges in the context of bar-driven evolution scenarios (e.g. Pfenniger & Norman 1990; Friedli & Benz 1993, 1995; Athanassoula 2003a).

We review existing bar diagnostics for edge-on disks in § 2 and describe the N-body simulations used throughout this paper in § 3. The basic stellar kinematic bar diagnostics are presented in § 4 along with their viewing angle dependence. § 5 and § 6 describe, respectively, the time evolution of the diagnostics (as the bar evolves) and their inclination dependence (for galaxies close to but not perfectly edge-on). We discuss the uniqueness of the bar diagnostics and compare them to existing observations in § 7, and our results are summarized in § 8.

2. Past Diagnostics

Kuijken & Merrifield (1995) first proposed to use the major-axis position-velocity diagrams (PVDs) of edge-on disks to detect bars in external galaxies (see also Kuijken 1996). PVDs show the density or luminosity of material as a function of projected radius and line-of-sight velocity, and they are easily obtained by long-slit (or integral-field) spectroscopy. Although the bar signatures they predicted were similar to those observed, the diagnostics turned out to be flawed (see Paper II; § 7.1), and we focus here on the improved diagnostics presented in Paper I and Paper II.

In Paper I, we used the periodic orbits in a standard family of barred disk potentials as building blocks to model real galaxies, using a simple recipe to populate them. The global structure of the corresponding PVDs, obtained for reasonable combinations of orbit families and different viewing angles, provides in itself a reliable bar diagnostic for edge-on disks. Particularly, gaps between the signatures of the different orbit families (as well as material in the so-called forbidden quadrants) follow directly from the inhomogeneous distribution of the orbits. The shape of the signature of the x_1 and x_2 orbit families constrains the viewing angle to the bar and, to a lesser extent, the mass distribution of the bar and disk.

In Paper II, the hydrodynamical simulations of Athanassoula (1992b) were used to study the gaseous PVDs of edge-on barred disks for various viewing angles and mass distributions, using the same family of potentials as for the orbits. Because of shocks and inflow in the bar region, a characteristic gap develops in the PVDs between the signature of the nuclear spiral (when an inner Lindblad resonance is present) and that of the outer disk. This is a clear bar diagnostic and the viewing angle is further constrained by the signature of the nuclear spiral. Those kinematic bar diagnostics were successfully applied by Merrifield & Kuijken (1999) and Bureau & Freeman (1999), but a continuous worry is whether the tracer used (e.g. Hα, [N II], CO, H I, etc) effectively samples the equatorial plane.

Although they are indicative of the gaseous and stellar structures to be expected from the PVDs of real galaxies, the above models are clearly not fully satisfactory. They are not self-consistent, and Paper I relies solely on periodic orbits, while regular (trapped) and chaotic orbits are expected to be important. Furthermore, both models are two-dimensional (2D) and are thus confined to the equatorial plane of the galaxies. This is not a major obstacle for the gas, which typically has a small scaleheight, but it is an unnecessary restriction for the stars, in particular if one wants to probe the potential to large galactic heights (as for B/PS structures) or non-exactly edge-on systems.

3. N-Body Models

3.1. Simulations

Naturally, the next step is to develop more reliable and realistic kinematic diagnostics for the stars, using self-consistent 3D N-body simulations. For this, we use N-body simulations similar to those discussed in Athanassoula & Misiriotis (2002). A large number of simulations were run and analyzed but only three representative cases are discussed here in details: weakly, intermediate, and strongly barred disks. They are shown in Figure 1 along with a simulation preserving axisymmetry.

Because a number of parameters influence the strength of a bar (e.g. the bar mass, length, axial ratio, radial density profile, etc), an exhaustive discussion of the whole of parameter space would be extremely lengthy and is in any case not necessary for our goals. The sequence chosen is thus meant to represent a growing influence of the bar on the entire disk, as reflected for example by its vertical extent, central concentration, and the contrast of the inner ring and outer spiral arms (or equivalently the depletion of material around the Lagrange points L_4 and L_5). The increasing bar strength in the simulations discussed is illustrated in Figure 2, which shows the importance of the even terms (compared to the axisymmetric term) in a Fourier decomposition of the face-on density distribution of each model (see also Athanassoula & Misiriotis 2002).

The initial conditions were set roughly following Hernquist (1993) and Athanassoula & Misiriotis (2002), and the simulations contain only a luminous disk and dark halo. No bulge is present, so all the quantities discussed in this paper refer exclusively to disk material, although as we will see much of it does acquire a large vertical extent.

The initial disk density is given by

$$\rho_{\rm d}(R,z) = \frac{M_{\rm d}}{4\pi h^2 z_0}\ \exp(-R/h)\ {\rm sech}^2(\frac{z}{z_0}), \tag{1}$$

where $M_{\rm d}$ is the total disk mass, h the disk radial scalelength, z_0 the disk vertical scaleheight, and R and z are respectively the cylindrical radius and height. For all barred simulations, $M_{\rm d} = 1$, $h = 1$, and $z_0 = 0.2$. The Q value is initially set to be constant throughout the disk at a value near unity. For the three barred simulations shown in Figure 1, $Q = 1.4$, 1, and 1 (from left to right).

The initial dark halo density is given by

$$\rho_{\rm h}(r) = \frac{M_{\rm h}}{2\pi^{3/2}}\,\frac{\alpha}{r_{\rm c}}\,\frac{\exp(-r^2/r_{\rm c}^2)}{r^2+\gamma^2}, \tag{2}$$

where $M_{\rm h}$ is the total halo mass, $r_{\rm c}$ and γ are halo scalelengths, r is the spherical radius, and α is a normalization constant. For all barred simulations, $M_{\rm h} = 5$ and $r_{\rm c} = 10$. In order to obtain bars of different strengths, we have followed the precepts of Athanassoula & Misiriotis (2002) and Athanassoula (2002, 2003a) and used halos with adequate parameters. For the strongest bar, $\gamma = 0.5$. This halo is relatively concentrated and has substantial mass in the region where the main resonances develop. This leads to a large angular momentum exchange between the halo and disk component and to a strong bar (Athanassoula 2002, 2003a). For the intermediate bar case, $\gamma = 3$, decreasing the halo mass in the resonant regions but ensuring sufficient angular momentum exchange to form a bar of intermediate strength. For the weak bar we ensured that the halo resonances could not absorb much angular momentum

by rendering the material there quite hot. In practice, this was achieved as in Athanassoula (2003a), i.e. by using an extended halo with twice the mass (see Athanassoula 2003a for details).

The left column in Figure 1 is included for comparison and shows a simulation in which the disk does not develop a bar. We used an artifact to achieve such stability, namely a rigid halo that by necessity can not exchange angular momentum with the disk. In this case, $M_\mathrm{d} = 0.3$, $h = 1$, $z_0 = 0.2$, and $Q = 0.1$. The halo parameters are $M_\mathrm{h} = 5$, $r_\mathrm{c} = 10$, and $\gamma = 0.5$. The disk thus remains stable, despite the fact that it is cold.

In all simulations, 2×10^5 particles are used for the disk, resulting in typically $0.9 - 1.0 \times 10^6$ particles for the halo. As shown by Athanassoula & Misiriotis (2002) and Athanassoula (2003a), angular momentum exchange between the disk and halo ensures that all barred simulations are more centrally concentrated and are luminous matter (i.e. disk) dominated in the inner parts at late times, no matter what the initial halo concentration is. The important characteristic of the three barred simulations selected is thus truly the strength of the bar at late times. Our analysis was actually carried out for a much larger sample of simulations than shown here (well over 100), but all of them possess features similar to those described in § 4–6, although of course the features' amplitudes vary from case to case. The following parameter space was carefully (but not systematically) explored: $Q = 0.1 - 2$, $\gamma = 0.5 - 5$, and $z_0 = 0.1 - 0.2$ (all other parameters were generally kept fixed).

All simulations were run on a Marseille Observatory GRAPE-5 system with a GRAPE treecode similar to that described in Athanassoula et al. (1998). An opening angle of 0.6 was used with a softening length of 0.0625 and a time step of 0.015625, resulting in an energy conservation better than or equal to 0.1% over the entire duration of the simulations (which are stopped at $t = 900$). Full information on all particles is saved every 20 time units (see § 5). Throughout the paper, the units used are such that $M_\mathrm{d} = 1$, $h = 1$, and $G = 1$. Thus, for a disk of mass 5×10^{10} $\mathrm{M}_\odot$ and scalelength 3.5 kpc, the unit of mass is 5×10^{10} $\mathrm{M}_\odot$, the unit of length is 3.5 kpc, the unit of velocity is 248 km s^{-1}, and the unit of time is 1.4×10^7 yr. To create FITS (Flexible Image Transport System) files (see below), we use a binning of 0.08 per pixel spatially and 0.125 in velocity. For the scalings above, this corresponds to 280 pc ($2\farcs9$) per pixel at a distance of 20 Mpc and a two-pixel spectral resolution of 62 km s^{-1} ($R = 4835$), similar to the typical set-ups used in stellar kinematic studies of nearby galaxies. To ensure a sufficient signal-to-noise ratio S/N in the outer parts when extracting the kinematics, we must use a slit width of 0.5, much thicker than normally used. We have verified that this make no qualitative and minimal quantitative differences to our results. We are however limited in our ability to derive the kinematics at large galactic heights, where the density drops rapidly, and a few simulations with greater numbers of

particles will be discussed at large z in Zamojski et al. (2005, in preparation), along with relevant observations. We thus limit ourselves here to the major-axis kinematics.

The simulations are manipulated with NEMO (e.g. Teuben 1995) and folded about the equatorial plane and under an 180° rotation to increases the S/N (analogous to assuming vertical and bi-symmetry). Long-slit spectra along the major-axis are then extracted into FITS files for further kinematic analysis, taking into account the necessary line-of-sight integrations. Those spectra are fed to the XSAURON data analysis software (Bacon et al. 2001; de Zeeuw et al. 2002), where the line-of-sight velocity distribution (LOSVD) at each position is fit with a Gauss-Hermite series. This is necessary because, as will be shown in § 4, the LOSVDs often deviate significantly from a Gaussian and much information is contained in the high and low velocity wings (see van der Marel & Franx 1993; Gerhard 1993). It also allows us to stick as closely as possible to observations, where absorption line (i.e. stellar kinematic) data are normally parametrized by Gauss-Hermite series. Although this requires high S/N, reliable profiles are now routinely available in the literature (at least up to h_3; e.g. Bender et al. 1994; Fisher 1997; Chung & Bureau 2004; Emsellem et al. 2004). The mean velocity V and velocity dispersion σ can be chosen to have their usual meanings, while the third (h_3) and fourth (h_4) order terms represent respectively the asymmetric (skewness) and symmetric (kurtosis) departures from a pure Gaussian. Clearly, however, the deconvolution step of observational data analysis (arguably the most sensitive) is neither necessary nor possible with N-body data. Furthermore, any comparison with real data must intrinsically assume a certain mass-to-light ratio M/L for all luminous N-body particles, which we take here as constant. This is probably a satisfactory assumption in the inner parts of galaxies (e.g. Kent 1986; Peletier & Balcells 1996) and at near-infrared wavelengths.

3.2. Relevance and Limitations

Both the initial conditions and the assumptions built in a pure N-body treatment are of course highly idealized. This holds not only for the simulations discussed here, but also for the vast majority of N-body simulations presented so far in the literature. In particular, such simulations start with quiet axisymmetric disks, with specific mass, velocity, and velocity dispersion radial profiles, and they do not include a gasous component. We will briefly discuss those assumptions here, before turning to a comparison of simulated and real bars.

Our initial conditions assume a sech^2 law for the vertical disk density and a halo with a core. We ran other simulations with an initial vertical slab geometry, with similar results. Athanassoula & Misiriotis (2002) and Athanassoula (2002, 2003a) also clearly showed that, even for highly concentrated and/or dominant halos, luminous matter can dominate the in-

ner parts of the models at late times. In fact, contrary to accepted wisdom, and as long as they are relatively cold, massive halos ultimately lead to stronger bars. Only few experimentations with a cosmologically-motivated (but still idealized) halo (Navarro, Frenk, & White 1996) have been reported so far (e.g. Valenzuela & Klypin 2003; Mayer & Wadsley 2004). The results of Valenzuela & Klypin (2003) are very similar to those of Athanassoula (2003a) with an extended halo, particularly regarding the bar length. Nevertheless, more thorough and quantitative comparisons are clearly required to fully assess the effect of cosmologically motivated halos on bar structure. The effect an initial bulge would have on disk particles is very much like that of a dark halo, although the bulge also directly affects observables. In particular, because of the superposition of the bulge, the apparent strength of any boxy or peanut shape resulting from disk thickening decreases (Athanassoula 2004). Some simulations with an initially radially varying Q parameter are discussed by Athanassoula (2003a), but no difference liable to change any of the results of the current paper was found.

Berentzen et al. (1998) have shown that the presence of gas in simulations tends to weaken both the bar and the B/PS bulge resulting from disk thickening. A substantial amount of gas is however required, making the process irrelevant for early and intermediate type spirals, and the central masses resulting form gaseous inflow are rather large. In any case, clear B/PS bulges are observed in gas-rich late-type galaxies (Lütticke et al. 2000a), questioning the true efficiency of such processes. Total bar disruption (e.g. Pfenniger & Norman 1990; Friedli & Benz 1993) is also in conflict with the large fraction of bars observed, unless they can be regenerated rapidly, which requires substantial external gas accretion (e.g. Bournaud & Combes 2002). The latter issue is still open observationally.

As for non-idealized initial conditions extracted directly from cosmological simulations of structure formation, while those simulations often include gas and simple recipes for star formation and evolution, the spatial and mass resolutions are usually too crude to study the dynamics of the systems in details. Thus, very few results on the dynamical evolution of disk substructures have been obtained by such simulations, in contrast to the wealth of results obtained with idealized models.

To summarize, while our simulations do have shortcomings, they allow a robust analysis and a well-grounded discussion. In particular, since many of the kinematic bar properties identified in this paper can be related to generic properties of orbits (see below), we believe that most of our results should also be generic.

As for a detailed comparison of our simulations (and similar ones) with real galaxies, one might think that our strong bar case seen nearly side-on yields a B/PS bulge more extreme than commonly observed in nearby galaxies (see, e.g., Fig. 1). However, a detailed look at a large sample of edge-on galaxies shows that this is not the case. While there are no statistics

on the incidence of "extreme" peanut-shaped bulges, Lütticke et al. (2000a) found that about 4% of all (edge-on) galaxies have a clear peanut-shape bulge (9% of all non-spheroidal bulges) and 20% have a clear box *or* peanut-shape bulge (44% of all non-spheroidal bulges). Those fractions are non-negligeable considering that peanut-shaped bulges are only observed for rather strong bars seen nearly side-on. Indeed, as the angle between the bar minor-axis and the line-of-sight increases, the apparent peanut strength decreases. As they are usually shown perfectly side-on, peanut-shaped bulges in simulations tend to appear more extreme than observed peanuts, which have various orientations. Perhaps most important, as mentioned above, the presence of a classical bulge in addition to a bar also decreases the apparent strength of the peanut toward a more boxy shape (e.g. Athanassoula 2004).

Some well-known extreme examples of B/PS bulges include IC 4767, first studied in detail by Whitmore & Bell (1988), but a very strong peanut-shaped bulge is also clearly seen in a number of objects from the Bureau & Freeman (1999) and Chung & Bureau (2004) sample, even in their poor quality optical Digitized Sky Survey (DSS) images. Examples include ESO151- G004, NGC 2788A, ESO443- G042, NGC 6771, ESO597- G036, and a number of weaker cases. The bulges' shapes are in fact even more extreme at K-band, generally considered a better tracer of the mass in spiral galaxies and unaffected by dust, as will be shown in Bureau et al. (2005) and Athanassoula et al. (2005). Better spatial resolution also usually yields sharper B/PS features, as is clearly illustrated by the Hubble Heritage image of ESO597- G036[1].

Other observational properties of B/PS bulges also tend to compare favorably with our or similar N-body simulations. No thorough comparative study exists, but a number of observables have been measured in both observations and simulations and several comparisons of specific properties have been made. Athanassoula & Misiriotis (2002) and Athanassoula (2003b) make a strong case that the behavior of their barred N-body models agrees well with observations of face-on barred galaxies, for quantities as varied as Fourier amplitudes of the mass distributions, surface brightness profiles, axial ratios, and isophotal shapes. Athanassoula (2004) extend those comparisons to edge-on systems, in particular using surface brightness cuts, median-filtered images, and velocity fields. A positive comparison of the kinematic properties of edge-on galaxies and the current simulations is provided by Chung & Bureau (2004) and in § 7.5.

---

[1]http://heritage.stsci.edu/1999/31/

4. Bar Diagnostics

In addition to the model with no bar, Figure 1 shows the stellar morphology and major-axis kinematics of the three selected simulations with a weakly, intermediate, and strongly barred disk, all viewed edge-on. The bars appear rather round when seen end-on (line-of-sight parallel to the bar), boxy or slightly peanut-shaped when viewed at intermediate angles, and strongly peanut-shaped when seen side-on (line-of-sight perpendicular to the bar; see Combes & Sanders 1981; Combes et al. 1990; Raha et al. 1991). All the bars could easily be confused with a "classical" bulge (i.e. a nearly axisymmetric, vertically extended structure containing no disk material) based on the photometry alone, although the simulations contain no such material. To provide the tools to discriminate between the two, we focus here on identifying characteristic signatures of triaxiality in the (projected) stellar kinematics.

4.1. Position-Velocity Diagrams

Although observed stellar PVDs are usually rather noisy, prompting a parametric description such as the Gauss-Hermite fits used here, the PVDs of Figure 1 contain a wealth of information which can be interpreted directly in orbital terms. For this, we rely heavily on the discussion of PVDs from individual periodic orbit families presented in Paper I, even though they were in 2D only (see Contopoulos 1980 and Contopoulos & Grosbøl 1989 for a more extensive descriptions of 2D orbit families). The orbit families in the N-body case can be viewed as a 3D generalization of those, and for simplicity we will hereby refer to the "trees" of orbit families related to the x_1 (elongated parallel to the bar) and x_2 (elongated perpendicular to the bar) orbits simply as x_1 and x_2 (see, e.g., Skokos et al. 2002a,b).

The PVDs of the axisymmetric case do not vary with viewing angle and their upper envelopes roughly follow the circular velocity curve, with a characteristic tail of low-velocity material ($h_3 - V$ anti-correlation) due to the projected outer disk. The PVDs of the strong bar case most clearly delineate the signatures of the different barred orbit families. Two families dominate. First, the x_1 orbits give rise to the central parallelogram-shaped feature in the PVDs (see Fig. 1). This particular shape arises because their axial ratio a/b increases with decreasing radius (a and b are, respectively, the semi-major and semi-minor axes), and the inner x_1 orbits reach correspondingly higher (along the major-axis) or lower (along the minor-axis) velocities compared to the outer ones (Paper I). Thus, when the bar is seen end-on, the parallelogram-shaped signature of the x_1 orbits reaches high line-of-sight velocities (particularly in the center) and has a small projected width. It thus appears thin (long and narrow). When the bar is seen side-on, the parallelogram-shaped signature of the x_1 orbits reaches only low projected velocities and has a large projected width, appearing fat (short

and wide). Generally however, the N-body signature of the x_1 orbits is wider than that predicted in Paper I, particularly when the bar is seen exactly end-on or side-on. This is expected since the orbits in the simulations are regular, i.e. trapped around stable periodic orbits, or chaotic. The current PVDs can thus be thought of as blurred versions of those in Paper I, in the same manner as the blurred periodic orbit distributions of Patsis et al. (2002) should roughly resemble real galaxies.

The second dominant feature of the PVDs is the bright almost solid-body feature which crosses the x_1 parallelogram in the central parts and becomes flat in the outer parts (Fig. 1). It is partly due to the orbits composing the inner ring (high order families within corotation; see Patsis et al. 2003b), but mostly to the multitude of stars and orbits beyond corotation (and seen in projection). The parent orbits are thus close to circles and their signature in the PVDs does not vary much with viewing angle. Because the orbits are not perfectly circular, however, their signature is not exactly solid-body but slightly curved (e.g. outer 2:1 orbits; see, again, Paper I).

It is interesting to note that we do not see much evidence for x_2 orbits. These should be most obvious in the PVDs when the bar is seen side-on (Paper I), but they are not observed (at least not in large numbers).

The superposition of the outer disk signature to that of the x_1 orbits (which is viewing angle dependent) is at the origin of most of the bar features observed in the PVDs, and thus in the Gauss-Hermite kinematic profiles (Fig. 1). As such, the latter can reliably be used both to identify the presence of a bar and to constrain its viewing angle. In particular, the x_1 orbits appear responsible for the tail of high velocity material ($h_3 - V$ correlation) observed at most viewing angles, which we argue is a good indicator of triaxiality. Those effects are discussed in details below.

4.2. Surface Brightness Profiles

Although not strictly speaking a kinematic quantity, the surface brightness profile along the major-axis can also be derived from kinematic observations, for example by summing long-slit data in wavelength. For the axisymmetric case, the surface brightness roughly follows an exponential profile, as expected from the initial conditions. For the strong bar case seen end-on, the bar appears as a prominent central peak in the light profile, with an approximately exponential but steep decline (see Fig. 1). A local minimum is created at moderate radii, followed by a slight rise up to the end of the bar (the inner ring; $X \approx 4.0$) and a smooth decline at larger radii. The inner ring is easily visible in both the strong and

intermediate bar cases. The local minimum becomes a broad “shoulder” at intermediate viewing angles and a truly flat plateau when the bar is seen side-on. This plateau can be identified with the plateaus often claimed to trace bars in the edge-on galaxy photometry literature (e.g. de Carvalho & da Costa 1987; Hamabe & Wakamatsu 1989; Lütticke et al. 2000b). The width of the central peak also increases slightly with viewing angle. Both the central peak and the shoulders/plateaus are still relatively strong in the intermediate bar case, but only the central peak remains prominent for the weak bar. This peak is testimony that a substantial radial rearrangement of material occurs, even for the weakest bars (see § 5).

A prominent and steep central peak with quasi-exponential light profile thus appears characteristic of bars in our models, although it would normally be associated with a classical bulge in standard bulge-disk decompositions (e.g. Andredakis, Peletier, & Balcells 1995; de Jong 1996; MacArthur, Courteau, & Holtzman 2003).

4.3. Velocity Profiles

As expected from the initial circular velocity curve of the model, the rotation curve of the axisymmetric case has a rapid but smooth rise and remains flat at large radii. As shown by the strongly barred case of Figure 1, however, the rotation curve of a barred disk seen end-on has a strong “double-hump” structure. That is, the rotation curve first rises rapidly and reaches a local maximum, it then drops slightly and creates a local minimum, and it rises again slowly up to its flat section. This behavior is weakened at intermediate viewing angles, when the local maximum and minimum disappear to form a single plateau at moderate radii. Once seen side-on, the disk rotation curve appears almost completely solid-body, with a steeper gradient just before the flat part. As expected, the double-hump structure is weakened for the intermediate bar case, where only broad plateaus are visible at moderate radii for all viewing angles. For the weak bar case, the double-hump structure has essentially completely disappeared.

For the barred cases, we note that the velocity reached by the rapidly rising part of the rotation curve (the first hump) decreases with increasing viewing angle, suggesting that this feature is caused by the (mostly inner) x_1 orbits. The radius at which the rotation curve becomes flat simultaneously increases, and it appears to mark the beginning of the inner ring, which is slightly elongated parallel to the bar (e.g. Athanassoula & Misiriotis 2002). In fact, the flat part of the rotation curve is usually reached at the end of the plateau in the light profile, while the local velocity minimum at moderate radii (or more generally the end of the first velocity plateau) occurs roughly at the end of the central luminosity peak (see

§ 4.2).

Whether or not there is a local maximum and minimum at moderate radii, a double-hump structure in the rotation curve appears characteristic of bars viewed edge-on (except for the weakest cases), although as we will argue below (§ 7.3) it is probably not uniquely related to them.

4.4. Velocity Dispersion Profiles

The velocity dispersion profile of the axisymmetric case is unusual but simply reflects the fact that the disk is very cold, the dispersion mainly resulting from the line-of-sight integration through the outer disk (the observed σ should in principle go to zero in the center for a perfectly cold disk). The velocity dispersion profile of the strong bar case seen end-on is also characteristic. Rather than a sharp central peak, the profile has a broad and rather flat central maximum followed by a sharp drop and a significant secondary (local) maximum. At intermediate and large viewing angles, the central peak is smaller, its decrement shallower, and the secondary maximum more important, such that a broad shoulder or plateau is formed at moderate radii (although a clear secondary maximum is still visible when the bar is seen side-on). For the intermediate bar case, only a narrow central peak is present, without a flat section, and the secondary peak is rather weak, again forming a shoulder or plateau at moderate radii. The viewing angle dependence is also much weaker. For the weakest bar case, only a central peak superposed on a much broader and shallow increment is present for all viewing angles. We note that those dispersion features were also seen by Athanassoula & Misiriotis (2002), where they are much stronger because only a thin strip of particles around the major-axis was considered (no line-of-sight integration).

At least for the strong bar case, the width of the central flat section of the dispersion profile is always roughly the same as that of the rapidly rising part of the rotation curve, suggesting that they have a common origin (x_1 orbits; see § 4.3). The extent of the central σ peak is also aproximately equal to that of the central light peak (§ 4.2). Finally, the secondary dispersion maximum always occurs just within the flat part of the rotation curve, suggesting that it has its origin towards the end of the bar, just inside the inner ring. This is most likely due to the tips of the last x_1 orbits and the inner $4:1$ orbits. In particular, x_1 orbits with loops around the major-axis are expected in strong bars (e.g. Athanassoula 1992a), causing a local increase in the velocity dispersion, strongest for bars seen side-on. The higher energy inner $4:1$ orbits have similar loops, which will increase σ for bars seen both side-on and end-on. Higher order orbit families within corotation may increase the dispersion somewhat (at all viewing angles), but they will mainly contribute to the excess

surface density in the inner ring (Patsis et al. 2003a,b).

We also note that for a strong bar, a large variety of orbital shapes is encountered, particularly along the major-axis. This leads to an increase in the observed velocity dispersion compared to face-on views, particularly when the bar is seen end-on. For weak bars or ovals, where the orbits are almost self-similar (i.e. concentric), the orbital variety is greatly diminished, as is the viewing angle dependance. The small local central velocity dispersion minimum observed for strong end-on bars will be discussed further in § 7.4.

Generally speaking, thus, one should expect a (sometime broad and rather flat) σ peak with a broad shoulder and/or a secondary maximum as the characteristic signature of a (strong) bar viewed edge-on. The velocity dispersion profile is also highly correlated with the major-axis surface brightness profile.

4.5. h_3 Profiles

As the PVDs of Figure 1 clearly show, the LOSVDs have a complex shape in the bar region, and the Gauss-Hermite terms h_3 and h_4 are necessary to provide a good description. For the axisymmetric case, h_3 is essentially always anti-correlated with V, as expected. For the strong bar case seen end-on, however, h_3 is correlated with V over the entire projected bar length, that is until the secondary maximum in σ or just inside the flat part of the rotation curve. At larger radii, the h_3 profile is anti-correlated with V for some distance before being correlated again. As the viewing angle is increased, the nature of the correlations does not change, but they become much weaker. For a bar seen side-on, the h_3 profile is almost flat. The $h_3 - V$ correlation over the projected bar length is relatively strong for the intermediate bar case and is greatly diminished but still present for the weak bar, which makes it a very good tracer of bars viewed edge-on.

The correlation of h_3 and V over the bar region is most likely a key tracer of triaxiality, although it is not uniquely related to it (see § 7.3). Indeed, for an axisymmetric disk viewed edge-on (or a slowly rotating spheroid), one would generally expect h_3 and V to be anti-correlated, since projection effects systematically create a tail of low-velocity material at each position. Only elongated motions (such as those of the x_1, 4 : 1, etc orbits) can create a tail of high velocity material, as required for h_3 and V to correlate. The viewing angle dependence of the $h_3 - V$ correlation can thus be traced to the viewing angle dependence of the (parallelogram-shaped) x_1 orbits signature in the PVDs (see § 4.1; Paper I).

For barred galaxies viewed exactly edge-on (such as the simulations of Fig. 1), the $h_3 - V$ correlation is strengthened by the superposition of the outer disk signature to that of the

x_1 orbits, which lowers the mean velocity (at all positions) and correspondingly "magnifies" the high velocity tail. The $h_3 - V$ correlation is then expected to be stronger if there is less material in the forbidden quadrants, which probably explains why the weak bar case still shows a significant signature (see, e.g., the a/b sequence in Paper II).

The situation is more complex for slightly inclined systems, where the outer disk is not necessarily seen (in projection), and for hot systems such as spheroids, where significant pressure support may be present. We discuss those issues in more details in § 6 and 7.3, respectively. Nevertheless, generally speaking, a correlation of h_3 and V appears characteristic of bars viewed edge-on.

4.6. h_4 Profiles

Although h_4 is hard to measure observationally, we discuss it here for completeness. For the strong bar seen end-on, a strong and rather flat minimum is present in the center, followed by a sharp rise and a more gentle decline at moderate radii. Those structures broaden and weaken substantially with increasing viewing angle, such that the h_4 profile is largely featureless at even moderate viewing angles. Weak features are visible for the intermediate bar case seen end-on, but for other viewing angles and for all viewing angles of the weak bar case, the h_4 profile is essentially flat.

At least for the strong bar case, the width of the central h_4 minimum is roughly the same as that of the flat part of the dispersion profile (and thus of the rising part of the rotation curve), perhaps a bit larger. In fact, h_4 and σ have roughly opposite behaviors. It is thus likely that all three features are due to the inner x_1 orbits.

4.7. Characteristic Bar Features

From the discussion above (Fig. 1), the characteristic kinematic signatures of bars viewed edge-on can be summarized as follows: 1) a quasi-exponential central peak in the surface brightness profile, with a shoulder or plateau at moderate radii; 2) a double-hump rotation curve, with or without a local maximum/minimum at moderate radii; 3) a possibly broad and rather flat central velocity dispersion peak, with a sharp edge and a shoulder or plateau (and possibly a secondary maximum) at moderate radii; 4) a correlation of h_3 and V over the projected bar length (i.e. within the flat part of the rotation curve). A local central σ minimum may also be present and the lengths of those features are not arbitrary, but correlated (see § 4.2–4.6).

The bar signatures tend to weaken as the viewing angle increases or the bar strength decreases, causing some degeneracy between the two. It should thus be relatively easy to kinematically identify an edge-on bar (unless it is very weak), but any constraint on the viewing angle will be rough at best. This parallels the situation for the gas (Paper II) and in our Galaxy (see e.g. Kuijken 1996 for a review). The light profile and rotation curve seem to be the most degenerate quantities, the velocity dispersion and h_3 profiles less so. In particular, the $h_3 - V$ correlation remains present even for weak bars. Clearly, whether one can actually disentangle bar strength from viewing angle will strongly depend on the quality of the data.

It is also interesting to note that the kinematic bar signatures are strongest when the bar is seen end-on and appears round, whereas it is easiest to identify bars morphologically when seen side-on because of the B/PS morphology. The kinematic and morphological methods are thus very much complementary, and they should permit to identify a bar if present in almost any edge-on system (unless it is very weak).

Lastly, it should be kept in mind the the concept of bar strength is somewhat ill-defined. Not only can a bar be strong in the inner parts and weak in the outer parts (or vice-versa), but many parameters influence the dynamics (e.g. bar axial ratio, mass, pattern speed, etc; e.g. Athanassoula 1992a,b). The kinematic features described above may therefore not all be present systematically in every object, but they should be considered separately, each individual feature yielding clues about the orbital structure.

The length of a bar is a similarly difficult quantity to measure precisely (e.g. Athanassoula & Misiriotis 2002), but many of the kinematic features present in the profiles of Figure 1 can be used as rough yardsticks. First, the end of the plateau in the major-axis light profile and the position where the rotation curve becomes flat both appear to trace the position of the inner ring. The secondary σ maximum, the end of the $h_3 - V$ correlation region, and the secondary h_4 minimum are also usually roughly equal although slightly shorter than the previous two quantities (more so for h_3), and they probably trace better the end of the bar itself. The exact location of all those features also depends somewhat on the orientation of the bar, reflecting the fact that most orbit families as well as the inner ring are elongated (e.g. Athanassoula & Misiriotis 2002). Nevertheless, if the location of corotation (or any other resonance) can be independently determined, those measurements of the bar length will provide useful constraints on the bar pattern speed in the usual dimensionless manner ($r_{\rm cr}/r_{\rm bar}$, where $r_{\rm cr}$ is the corotation radius and $r_{\rm bar}$ the radius of the bar).

5. Time Evolution

For the strong bar case only, Figure 3 shows the complete time evolution of the various major-axis kinematic profiles (μ_I, V, σ, h_3, and h_4), from the initial conditions through bar formation and buckling to the end of the simulation. The stellar distribution changes rapidly and has high order structures ($m > 2$) early on ($t \lesssim 160$). Bar formation occurs at $t \approx 180 - 240$ and buckling at $t \approx 260 - 320$, while significant vertical asymmetries persist until $t \approx 440$. From then on, the evolution is smooth but continous. We look at the temporal behavior of each kinematic quantity individually below, but after bar formation the general trend is that, like the bar itself, most kinematic bar signatures grow in strength and length with time. This is expected because, as the bar lengthens, the various orbit families and their associated signatures do so as well. The bar growth and lengthening is most likely due to a transfer of angular momentum from the disk to the halo and is explored further in Athanassoula (2002, 2003a).

The moment the bar forms, the material in the disk is substantially rearranged and a quasi-exponential central peak develops in the surface brightness profile. For all viewing angles, the intensity of the central peak grows with time, simultaneously with the flatness of the plateau at moderate radii and the intensity of the secondary maximum (if present). The extents of the central peak and plateau also grow with time as the bar lengthens.

For the rotation curve, the central part steepens significantly during bar formation and the double-hump structure establishes itself fairly rapidly. Once formed, the rapidly rising part of the rotation curve does not change much. The velocity plateau at moderate radii, however, stretches with time and becomes an increasingly deep local minimum. The radius at which the rotation curve becomes flat simultaneously increases. The same is true at all viewing angles, with the caveat that the features are generally weaker with increasing viewing angle (see § 4). The characteristics bar signatures in the velocity profile thus increase in strength and length with time, except in the inner parts.

The central peak in the velocity dispersion profile steepens and increases dramatically during bar formation. The local minimum and secondary maximum at moderate radii appear soon after and their strength and distance from the center increase with time. Again, the evolution is roughly the same at all viewing angles although the features are weaker for large viewing angles (§ 4). Interestingly, the width of the central peak does not change much for end-on views, but it does grow slightly for side-on views, suggesting that only the length of the bar but not its width is increasing. The peak value increases throughout. The central dip in the dispersion peak at $t = 0$ is probably a consequence of the approximations involved in the asymmetric drift correction for the inner parts (when setting up the initial conditions; see Hernquist 1993) and of the fact that the disk is initially rather cold kinematically (see

§ 3.1 and 4.4). As the local minimum disappears when the disk slushes around at early times and the bar forms, we are confident that the σ behavior at later times is genuine.

The time evolution of the h_3 profiles is very simple. For all viewing angles, both the central region where h_3 correlates with V, the following $h_3 - V$ anti-correlation region, and the outside region where h_3 correlates with V again all grow in length with time. The gradients become slightly more shallow, however. The initial $h_3 - V$ correlation within 0.5 disk scalelength is probably again an artefact of the (imperfect) asymmetric drift correction at $t = 0$. It weakens at early times and disappears totally during bar formation and buckling, only to reappear once the bar is fully formed ($t \approx 320$), so the h_3 behavior at later times is reliable.

Analogous to the σ evolution, the central minimum in h_4 grows with time, although it is truly the amplitude of the secondary maximum which increases. Furthermore, while the width of the central minimum remains largely unchanged as the bar evolves, the width of the secondary maximum increases. The same behavior is observed for all viewing angles, but the profiles are almost featureless for even moderate ones (see § 4.6). The central maximum at $t = 0$ disappears soon after the bars forms and should not affect the subsequent bar evolution.

6. Inclination Dependence

It is essential to understand how the kinematic bar signatures identified vary with the inclination i, for two main reasons. First, the signatures are likely to depend sensitively on i, as the line-of-sight integration through the outer disk (which acts like a kinematic "screen") decreases significantly even for moderate offsets. Second, optical observations of intermediate and late-type spirals usually call for close to but not exactly edge-on systems, as thick dust lanes are common and prevent the line-of-sight from reaching the central parts of the galaxies in perfectly edge-on objects. This is well illustrated by the work of Chung & Bureau (2004).

Figure 4 shows the inclination dependence of the major-axis kinematic profiles for the strong bar case. For a bar seen end-on, the value of the central peak in the surface brightness profile varies little with i, but its prominence increases as i decreases (from 90°, i.e. exactly edge-on, to lower values). This is because the level of the plateau at moderate radii decreases as the low density regions on the minor-axis of the bar (around the Langrangian points L_4 and L_5) become exposed. This effect is thus much weaker for intermediate viewing angles (although a break appears at the end of the bar), and it is almost absent when the bar is

seen side-on.

For an end-on bar, the central gradient in the rotation curve steepens (and the maximum velocity reached increases) as i decreases. This is because the moderating influence of the outer disks decreases and the x_1 orbits (also seen end-on) are more fully exposed. The effect is easily seen in the PVDs of Figure 4, where the quasi solid-body contribution of the (projected) outer disk to the PVDs gradually disappears as i decreases, resulting in higher mean velocities. The effect is of course opposite for large viewing angles, where the the bar and the x_1 orbits are seen more side-on. There, the central gradient in the rotation curve becomes much shallower, and the velocity profile shows a sharp break at the end of the bar (connecting to the flat part of the rotation curve).

The velocity dispersion profile is also strongly affected by the gradual disappearance of the (projected) outer disk as i decreases. For end-on views, although the value of the maximum does not change, the width of the central peak widens dramatically (essentially to the width of the bar itself) and its edges become sharper (almost a step function). For intermediate and large viewing angles, the width of the central peak changes little but the edges also become sharper. In fact, the most important change is the increase of the secondary σ maximum at moderate radii, which reaches values comparable to that of the central peak for "small" inclinations (e.g. $i = 75°$). This is probably testimony to the large vertical motions of the orbits near the end of the bar, as shown by Skokos et al. (2002a,b) and Patsis et al. (2002), and to the loops and large rectangularity of the x_1 and 4:1 orbits in that region. In fact, for side-on views, as the inclination is decreased, the slit encompasses only material increasingly near the major-axis of the bar, and this material is known to have a dispersion similar to that shown in Figure 4 (Athanassoula & Misiriotis 2002).

Surprisingly, while for perfectly edge-on systems the $h_3 - V$ correlation decreases with increasing viewing angle, the opposite is true for objects significantly less inclined ($i \lesssim 80°$). For a bar seen end-on, the $h_3 - V$ correlation decreases as i decreases, and there is in fact a slight anti-correlation for $i \lesssim 80°$. As shown by the PVDs of Figure 4, this is because as i decreases and the PVD signature of the (projected) outer disk disappears, the mean velocities increase (see above) and the asymmetric tail of material in the LOSVDs switches from high to low velocities. For large viewing angles, however, when the bar and the x_1 orbits are seen more side-on, the mean velocities actually decrease with decreasing i (again, see above), and the tail of material in the LOSVDs remains at high velocities (especially toward the ends of the bar).

For bars seen end-on, where most of the structure in the h_4 profile is observed (see § 4), the shape of the central parts of the profile remain largely unchanged as i decreases, although all the values themselves decrease. This leads to a wide and deep central minimum with a

small and sharp central peak at small inclinations. The h_4 profiles are still rather featureless at intermediate and large viewing angles, although a sharp break develops at the end of the bar for small inclinations.

7. Discussion

7.1. Orbit Populations

While the PVDs of Paper I were generated by selecting orbits equally spaced along the bar minor-axis, a much better fit to the N-body PVDs (at least for the x_1 orbits) is obtained by selecting orbits with an equal increment of the Jacobi integral $E_{\rm J}$ ($E_{\rm J} = E - \Omega_{\rm p} J_{\rm z}$ is the only conserved quantity in a barred galaxy, where $\Omega_{\rm p}$ is the pattern speed of the bar and $J_{\rm z}$ the angular momentum along the axis of revolution). Such models were briefly discussed in Paper I but no PVD was shown. The characteristic curve of the x_1 orbits (semi-minor axis vs. $E_{\rm J}$) is typically composed of two sections: a first rather flat section where the semi-minor axis barely changes for large increments in $E_{\rm J}$, and a second almost vertical section where the semi-minor axis increases very rapidly for just a small $E_{\rm J}$ increment (see, e.g., Athanassoula 1992a; Paper I). Our results thus imply that the first section of the x_1 characteristic is preferentially populated. This is not entirely surprising, since we have shown that a steep density gradient develops at the center of our models (e.g. Fig. 3), implying that the inner x_1 orbits are substantially more populated than the outer ones.

We also note that no "figure-of-eight" is observed in the stellar PVDs, under any circumstance (see Figs. 1–4). This bar diagnostic was popularized by Kuijken & Merrifield (1995) but results from a very selective population of the periodic orbits (no overlapping or self-intersecting orbits, particularly near corotation, and only a few outer 2 : 1 orbits; see also Merrifield 1996). Our models show that no such figure arises for realistic orbital configurations. Using simulations undergoing analogous bar-driven evolution, a similar conclusion was reached by O'Neill & Dubinski (2003), but they failed to identify alternative bar signatures. Contrary to their claim, observational techniques can be used with $\sim 10^6$ particle simulations, if the right tools are used. As shown in Paper II, a figure-of-eight feature can develop in gaseous PVDs, but only for very strong bars, and only extending to corotation (i.e. it arises from x_2 orbits and the inner ring, rather than x_1 orbits and an outer ring as advocated by Kuijken & Merrifield 1995). These results appear confirmed by observations (Kuijken & Merrifield 1995; Merrifield & Kuijken 1999; Bureau & Freeman 1999; Chung & Bureau 2004).

7.2. Central Light Peak and Freeman Type II Profiles

Independently of the issue of their 3D shape, so-called secular evolution scenarios for bulge formation have recently gained much momentum from the realization that many (and perhaps most) bulges have central light profiles more closely resembling a disk-like exponential than an $R^{1/4}$ law (expected from violent relaxation), with a tight correlation between the scalelengths of the bulge and disk (e.g. Andredakis et al. 1995; de Jong 1996; MacArthur et al. 2003; Balcells et al. 2003; see also Kormendy 1993). As illustrated in Figure 3, bar formation and evolution is accompanied by the development and continued growth of a very dense (but still slightly elongated) central component within $1 - 1.5$ original disk scalelengths (see also Athanassoula & Misiriotis 2002; Athanassoula 2002). In our major-axis surface brightness profiles (Figs. 1–4), this component would invariably be identified with a bulge, although there is no such material to start with in our simulations. Certainly, the central peak meets the fairly general definition of a bulge as the component in excess of the inward extrapolation of the outer exponential disk (e.g. Carollo, Ferguson, & Wyse 1999). Morever, Figs. 1–4 show that the shape of the central profiles is very close to exponential, so it seems natural to associate these central peaks, and thus bars, with the quasi-exponential bulges observed in more face-on systems (Athanassoula 2004). Although this will be more fully investigated in a future paper (Athanassoula et al. 2005), it is also interesting to note that in all but the weakest bar cases, the central parts of the bar appear to have a smaller scaleheight than the outer parts, leading to the characteristic peanut shape when the bar is viewed edge-on.

Most of the (edge-on) major-axis surface brightness profiles from our simulations would qualify as Freeman Type II profiles (Freeman 1970), having inner disks well below the inward extrapolation of the outer exponential. Our simulations clearly show that Type II profiles arise from both a radial and vertical redistribution of material (and to a lesser extent azimuthal), the stars in the barred region simultaneously moving in radially (due to angular momentum exchange with the halo; e.g. Athanassoula 2002, 2003a) and out vertically (due to vertical instabilities and the creation of the B/PS bulge). Obviously, only the first mechanism is relevant for face-on systems. The complicated surface bightness profiles of our models therefore do not stem from the presence of multiple decoupled morphological or dynamical components, but rather from the fact that the instabilities and resonances generated by the bar lead to a redistribution of the disk material, and local modifications of its scalelength and scaleheight.

Our simulations therefore suggest a close link between Freeman Type II profiles and bars, but this link is not entirely borne out by observations. Although barred galaxies are more likely to harbor Type II profiles, bars appear insufficient. They are perhaps even

unnecessary. Indeed, not all face-on barred galaxies have type Type II profiles, and some non-barred galaxies do (e.g. Baggett, Baggett, & Anderson 1996; MacArthur et al. 2003). Type II profile formation through bar-driven evolution thus seems to require that at least some bars be destroyed (while roughly maintaining their azimuthally-averaged profile). While possible, the efficiency of such mechanisms is questionable (e.g. Shen & Sellwood 2004; Athanassoula, Dehnen, & Lambert 2003 and references therein). The above observational studies were based on optical studies, however, and it is known that the fraction of barred disk galaxies increases in the near-infrared (NIR; e.g. Seigar & James 1998; Eskridge et al. 2000). It would thus be worthwhile to redo the statistics with NIR data, and see if the correlation between Type II profiles and bars gets stronger.

In any case, while a proper comparison of our models with observations is required, including full bulge-disk decompositions for a variety of disk orientations, our model light profiles clearly support the interpretation that many bulges are formed through bar-driven rearrangement of disk material. The exact nature of Freeman Type II profiles remains to be determined.

7.3. $h_3 - V$ (Anti-)Correlation

It is likely that the kinematic bar signatures discussed for I, V, and σ can individually be created by carefully selected axisymmetric density distributions or distribution functions. However, whether this remains true when all the signatures are considered simultaneously is unclear. Furthermore, the behavior of h_3 is generally less well understood, particularly with respect to V, so we consider some toy models below. Our goal is to understand under which axisymmetric conditions an $h_3 - V$ correlation can arise, and thus invalidate its use as a triaxiality diagnostic.

We first consider a kinematically cold axisymmetric disk, and assume a monotonically decreasing surface density profile. Such a disk can be thought of as a sum of circular rings, each yielding a straight line in an edge-on PVD (from the origin to the circular velocity at the ring's radius). Because of the decreasing surface density, the LOSVD at each (projected) position will systematically have a steep prograde wing and a tail of low-velocity material, yielding the usual $h_3 - V$ anti-correlation expected from an inclined disk. If the disk is inwardly truncated, the rotation curve will be solid-body until the inner ring's radius and then follow the circular velocity curve, and the $h_3 - V$ anti-correlation will be little affected. Adding an outwardly truncated inner disk (i.e. creating a double-disk structure), the velocity profile will become doubly peaked, but h_3 and V will remain anti-correlated at all radii, with perhaps a break at the end of the inner disk.

We can try relaxing the constraint on the surface density and consider a disk which is not strictly inwardly truncated, but rather has a lower surface density in the inner parts. Then, in the edge-on PVD, the mean velocity will be dictated by the (projected) outer disk and the inner disk will create a tail of high-velocity material, possibly yielding a correlation of h_3 and V without the need for triaxiality (if the high velocity tail of the inner disk is more important that the low-velocity one associated with the outer disk). This situation is similar to that of a strong bar seen end-on, as described in § 4.5, but there is no reason to expect such an ab initio density profile in a kinematically cold axisymmetric disk (although it can not be ruled out either). Truncated or double-disk structures can however arise from the influence of a bar, and it is often argued that their occurence in an axisymmetric galaxy indicates the past presence of a bar long dissolved or destroyed (see, e.g., Baggett et al. 1996; Emsellem et al. 1996; van den Bosch & Emsellem 1998). The same can thus perhaps be said of an $h_3 - V$ correlation.

A more interesting situation occurs if we consider an axisymmetric but kinematically hot subsystems at the center of our cold disk. This classical bulge-like component will have a mean velocity lower than the circular velocity (because of pressure support), but if taken in isolation will still yield an $h_3 - V$ anti-correlation when viewed edge-on. The same will be true if present within a truncated disk, although the rotation curve will then likely be double-peaked. If this classical bulge is inserted within a full disk, however, it is likely that the exact behavior of h_3 will depend on the bulge-to-disk ratio B/D. At any given (projected) position, the mean velocity could be dictated by the classical bulge if it is bright enough, the (projected) disk then creating a tail of high-velocity material, or the inverse may be true if the bulge is faint. Both $h_3 - V$ correlations and anti-correlations can thus probably occur as a function of (projected) radius and B/D (significant h_4 should also be expected). In fact, van der Marel & Franx (1993) showed that simple spherically symmetric and isotropic models can yield both $h_3 - V$ correlations and anti-correlations depending on the amount of rotation. In particular, h_3 was found to correlate with V for maximally rotating models (see also Gerhard 1993 for non-rotating models).

It is thus clear from the above that an $h_3 - V$ correlation is not uniquely related to triaxiality. It is possible that it simply traces a high surface brightness region with increased velocity dispersion (i.e. a spheroid-like component) embedded within a disk, whether triaxial or not. But it is unclear if any axisymmetric configuration could simultaneously account for all of the kinematic bar signatures observed (and their spatial correlations) in addition to h_3 (e.g. surface brightness plateau at moderate radii, double-hump rotation curve, flat-top or slightly peaked velocity dispersion profile with a secondary maximum and/or local central minimum, etc.). Although it is beyond the scope of this paper to prove the contrary, this appears rather unlikely since most of the features are directly related to the particular orbital

structure of barred disks. The kinematic bar signatures discussed throughout this paper are thus not only consistent with the presence of a bar, but they strongly argue for it.

Kinematic profiles derived from axisymmetric models with varying B/D would be useful to clarify the relationship of h_3 with the intrinsic shape of spheroids and the degree of pressure support. If the S/N of data is high enough, however, the PVDs themselves should allow to break any degeneracy, since they will be significantly different for the various configurations discussed (despite yielding qualitatively similar Gauss-Hermite parameters). In future work, we will study simulations which include a luminous axisymmetric bulge in addition to the current luminous disk and dark halo. This should allow us to quantify the effects of having a classical bulge in addition to a barred disk.

7.4. Central Velocity Dispersion Minima

As noted in § 4.4 and visible in Figures 1–4, a central velocity dispersion minimum is often present for strong bars seen approximately end-on. This is very interesting since central σ minima are generally associated with fast rotating (i.e. kinematically cold) disks, thought to form by gas inflow and subsequent star formation (whether bar-driven or not; e.g. Heller & Shlosman 1994; Friedli & Benz 1995). Here, however, the central σ minimum must arise from purely dissipationless processes.

Although the axis ratio a/b of the dominant x_1 orbits in bars generally increases with decreasing radius, this behavior is inverted near the center where the orbits become progressively more circular (although they can still be very elongated; see, e.g., Athanassoula 1992a; Paper I). This property is probably the main driving mechanism behind the central σ minima observed in our simulations. The relative shallowness of the minima is likely due to the facts that the bar density is not homogeneous in the inner parts and the axial ratio need not tend to 1 until very close to the center. The line-of-sight integration through the outer parts of the bar and disk must of course also be considered.

Although the central σ minimum for the strong bar case discussed here is comparable to those observed in the sample of Chung & Bureau (2004), it is probably shallower than the deepest central stellar velocity dispersion minima known (e.g. NGC 6503, Bottema 1989 and Bottema & Gerritsen 1997; NGC 1365, Emsellem et al. 2001). While gaseous processes clearly can not be neglected in those cases, we recall that we have not attempted to fit any particular object, and other stellar processes can also increase a purely stellar central σ minimum. For example, the central density profile can be less peaked (i.e. more homogeneous) and the bar (and orbits) axial ratio can decrease more rapidly in the inner parts. This is

particularly likely as the central a/b profile of the simulations is generally flatter than in real bars (see Athanassoula & Misiriotis 2002; Gadotti & de Souza 2003). Gas inflow will futher help, first by circularizing the potential in the inner parts, and second by adding a kinematically cold population of young stars if star formation occurs.

7.5. Observations

Chung & Bureau (2004) provide an in-depth comparison of theirs and other observations with our simulations, but we summarize here some important facts. Chung & Bureau (2004) obtained optical stellar kinematics along the major-axis for a sample of 30 edge-on spiral galaxies (S0–Sbc), 80% of which have a B/PS bulge. For essentially all B/PS bulges where the data are good enough, the predicted kinematic signatures are observed: double-hump rotation curves with a dip or plateau at moderate radii, often flat-top velocity dispersion profiles with a secondary maximum or shoulder, and h_3 profiles correlated with V over the expected bar length. Examples include the well-studied galaxies NGC 128, NGC 1381, and IC 4767, all perfectly edge-on and largely dust-free S0s with a B/PS bulge, as well as the later type spirals NGC 5746, NGC 6722, and NGC 6771. Furthermore, 40% of the galaxies have a local central σ minimum, and essentially no bar signature is observed in the non-B/PS bulges. The light profiles show a variety of shapes, but this is not surprising given that many galaxies are dusty. The K-band data of Bureau et al. (2005) will yield a more useful comparison (see also Aronica et al. 2003).

Fisher (1997) also present the stellar kinematics of a number of edge-on galaxies. Again, all B/PS bulges show the expected kinematic signatures. Two non-B/PS bulges also do, but they are consistent with bars seen end-on. The observations of NGC 4762 are particularly interesting in this respect. NGC 4762 is an edge-on S0 galaxy with a small round bulge and at least two extended plateaus in its major-axis surface brightness profile (Burstein 1979; Tsikoudi 1980; Wakamatsu & Hamabe 1984). It however appears very thin over the first plateau, traditionally associated with a bar, which has prompted speculation that either the bar is thin (i.e. it has not buckled) or the plateau is not related to a bar at all (e.g. Wozniak 1994). However, within the radial range probed by our simulations, both the morphology, photometry, and stellar kinematics are perfectly consistent with that expected for an end-on bar. In fact, Fisher's (1997) data are almost a perfect match to our generic simulation of a strong bar seen end-on, as shown in Figure 1. Similar cases include NGC 4350 (Fisher 1997) and IC 5096 (Chung & Bureau 2004).

A number of the (presumably) barred galaxies in the Fisher (1997) and Chung & Bureau (2004) samples also show an $h_3 - V$ anti-correlation in the very center, contrary to what is

observed here. This implies the presence of an additional central rapidly rotating component. Given that many of those galaxies also possess a gaseous nuclear spiral (Bureau & Freeman 1999), it is natural to postulate that this component arises from a younger and kinematically cold stellar population, presumably formed through bar-driven inflow and star formation (e.g. Heller & Shlosman 1994; Friedli & Benz 1993, 1995). Our simulations simply do not take into account this potential dissipative component. As discussed above (§ 7.4), it will contribute further to the central σ minimum observed in some galaxies.

The stellar kinematic observations of Fisher (1997) and Chung & Bureau (2004) are thus entirely consistent with our simulations and support the interpretation that B/PS bulges are indeed thick bars. Interestingly, signatures similar to the ones predicted here are also observed in more face-on barred systems, as illustrated by the double-hump rotation curves and central σ minima observed by Emsellem et al. (2001) in 4 moderately inclined intermediate-type spirals. 2D kinematic fields from wide-field integral-field spectrographs such as SAURON (Bacon et al. 2001) will provide the next level of tests, along with a full 2D analysis of N-body simulations (including higher order LOSVD terms), but preliminary results support both the above long-slit work and our current simulations (e.g. de Zeeuw et al. 2002; Bureau et al. 2002a,b; Emsellem et al. 2004). Improved morphological studies should also follow, and those will be provided by the K-band observations of the Chung & Bureau (2004) sample (Bureau et al. 2005; Athanassoula et al. 2005) and by parallel work on the current simulations.

8. Conclusions

To constrain bar-driven evolution scenarios for the formation of bulges, and more specifically to provide tools to probe the nature of boxy and peanut-shaped (B/PS) bulges, we have used self-consistent 3D N-body simulations of bar-unstable disks to study the kinematic signatures of edge-on bars. Quantifying the major-axis stellar kinematics with Gauss-Hermite polynomials, a number of features can be used as bar diagnostics: 1) a steep quasi-exponential central light profile with a shoulder or plateau at moderate radii; 2) a double-hump rotation curve, possibly showing a local maximum and minimum at moderate radii; 3) a sometime broad central velocity dispersion peak with a shoulder or plateau (and possibly a secondary maximum) at moderate radii; 4) line-of-sight velocity distributions (LOSVDs) with a high-velocity tail (i.e. an $h_3 - V$ correlation) over the projected bar length. A local central σ minimum can also be present for strong bars seen approximately end-on. The positions and lengths of those features are further correlated, providing an easy and reliable tool to identify bars in edge-on disks. We note that despite previous claims, a “figure-of-eight” is never seen

in stellar position-velocity diagrams (PVDs), as expected from realistic models and orbital configurations.

Interestingly, while some of the kinematic bar features can individually be created by axisymmetric density distributions, the $h_3 - V$ correlation appears to be a particularly reliable tracer of triaxiality (although it is not uniquely related to it). A number of those kinematic bar signatures can also be used as proxies for the bar length, and thus as an indirect measure of the bar pattern speed. The sharpness of the kinematic features generally decreases for weaker bar and/or increasing viewing angle (from end-on to side-on), introducing some degeneracy between the two but ensuring complementary with morphological bar signatures (strongest for side-on bars). All characteristic features of the kinematic profiles are established the moment the bar forms and grow stronger with time, as the bar lengthens and strengthens. They vary little for small inclination variations but noticeable differences appear for $i \lesssim 80°$.

Existing data and the recent work of Chung & Bureau (2004) show that most B/PS bulges indeed show the kinematic signatures identified here, lending support to evolution scenarios where those bulges are formed through vertical disk instabilities. Detailed work on the morphological and photometric properties of both simulated and observed B/PS bulges are ongoing (Bureau et al. 2005; Athanassoula et al. 2005) and should provide more tests of the consistency of these scenarios. Preliminary results support our current conclusions.

The current simulations also systematically produce Freeman Type II (truncated) surface brightness profiles with approximately exponential peaks, as is observed in most bulges (at least late-types). The local central σ minimum present in the strongest bars (and produced without dissipation) is also increasingly thought to be common in spirals.

Support for this work was provided by NASA through Hubble Fellowship grant HST-HF-01136.01 awarded by the Space Telescope Science Institute, which is operated by the Association of Universities for Research in Astronomy, Inc., for NASA, under contract NAS 5-26555. EA thanks J. C. Lambert for his help with the GRAPE software and the administration of the simulations. EA also thanks the INSU/CNRS, the University of Aix-Marseille I, the Region PACA, and the IGRAP for funds to develop the GRAPE and Beowulf computing facilities used for the simulations and their analysis. We wish to thank K. C. Freeman for his involvement in the early stages of this project as well A. Bosma, A. Chung, K. Kuijken, and R. van der Marel for useful discussions.

REFERENCES

Andredakis, Y. C., Peletier, R. F., & Balcells, M. 1995, MNRAS, 275, 874

Aronica, G., Athanassoula, E., Bureau, M., Bosma, A., Dettmar, R.-J., Vergani, D., & Pohlen, M. 2003, Ap&SS, 284, 753

Athanassoula, E. 1992a, MNRAS, 259, 328

Athanassoula, E. 1992b, MNRAS, 259, 345

Athanassoula, E. 2002, ApJ, 569, 83

Athanassoula, E. 2003a, MNRAS, 341, 1179

Athanassoula, E. 2003b, in Astrophysical Supercomputing Using Particles, eds. J. Makino and P. Hut (ASP: San Francisco), 177

Athanassoula, E. 2005, MNRAS, in press

Athanassoula, E., Aronica, G., & Bureau, M. 2005, MNRAS, submitted.

Athanassoula, E., Bosma, A., Lambert, J. C., & Makino, J. 1998, MNRAS, 293, 369

Athanassoula, E., & Bureau, M. 1999, ApJ, 522, 699 (Paper II)

Athanassoula, E., Dehnen, W., & Lambert, J.-C. 2003, in Highlights of Astronomy 13, ed. O. Engvold, 355

Athanassoula, E., & Misiriotis, A. 2002, MNRAS, 330, 35

Bacon, R., et al. 2001, MNRAS, 326, 23

Baggett, W. E., Baggett, S. M., & Anderson, K. S. J. 1996, in Barred Galaxies, eds. R. Buta, D. A. Crocker, & B. G. Elmegreen (San Francisco: ASP), 91

Balcells, M., Graham, A. W., Domìnguez-Palmero, L., & Peletier, R. F. 2003, ApJ, 582, L79

Bender, R., Saglia, R. P., & Gerhard, O. E. 1994, MNRAS, 269, 785

Berentzen, I., Heller, C. H., Shlosman, I., & Fricke, K. J. 1998, MNRAS, 300, 49

Binney, J., Gerhard, O. E., Stark, A. A., Bally, J., & Uchida K. I. 1991, MNRAS, 252, 210

Bottema, R. 1989, A&A, 221, 236

Bottema, R., & Gerritsen, J. P. E. 1997, MNRAS, 290, 585

Bournaud, F., & Combes, F. 2002, A&A, 392, 83

Bureau, M., Aronica, G., Athanassoula, E., Bosma, A., Dettmar, R.-J., & Freeman, K. C. 2005, MNRAS, submitted.

Bureau, M., & Athanassoula, E. 1999, ApJ, 522, 68 (Paper I)

Bureau, M., et al. 2002a, in Galaxies: The Third Dimension, eds. M. Rosado, L. Binette, & L. Arias (ASP: San Francisco), 208

Bureau, M., et al. 2002b, in The Dynamics, Structure & History of Galaxies, eds. G. S. Da Costa & H. Jerjen (San Francisco: ASP), 53

Bureau, M., & Freeman, K. C. 1999, AJ, 118, 126

Burstein, D. 1979, ApJS, 41, 435

Carollo, C. M., Ferguson, H. C., & Wyse, R. F. G. 1999, The Formation of Galactic Bulges (CUP: Cambridge)

Chung, A., & Bureau, M. 2004, AJ, 127, 3192

Combes, F., Debbasch, F., Friedli, D., & Pfenniger, D. 1990, A&A, 233, 82

Combes, F., & Sanders, R. H. 1981, A&A, 96, 164

Contopoulos, G. 1980, A&A, 81, 198

Contopoulos, G., & Grosbøl, P. 1989, A&A Rev., 1, 261

de Carvalho, R. R., & da Costa, L. N. 1987, A&A, 171, 66

de Jong, R. S. 1996, A&AS, 118, 557

de Souza, R. E. & dos Anjos, S. 1987, A&AS, 70, 465

de Zeeuw, P. T., et al. 2002, MNRAS, 329, 513

Eggen, O. J., Lynden-Bell, D., & Sandage, A. R. 1962, ApJ, 136, 748

Emsellem, E., Bacon, R., Monnet, G., & Poulain, P. 1996, A&A, 312, 777

Emsellem, E., Greusard, D., Combes, F., Friedli, D., Leon, S., Pécontal, E., & Wozniak, H. 2001, A&A, 368, 52

Emsellem, E., et al. 2004, MNRAS, 352, 721

Eskridge, P. B., et al. 2000, AJ, 119, 536

Fisher, D. 1997, AJ, 113, 950

Freeman, K. C. 1970, ApJ, 160, 811

Friedli, D., & Benz, W. 1993, A&A, 268, 65

Friedli, D., & Benz, W. 1995, A&A, 301, 649

Gadotti, D. A., & de Souza, R. E. 2003, ApJ, 583, 75

Gerhard, O. E. 1993, MNRAS, 265, 213

Heller, C. H., & Shlosman, I. 1994, ApJ, 424, 84

Hamabe, M., & Wakamatsu, K. 1989, ApJ, 339, 783

Hernquist, L. 1993, ApJS, 86, 389

Jarvis, B. J. 1986, AJ, 91, 65

Kent, S. 1986, AJ, 91, 1301

Kormendy, J. 1993, in Galactic Bulges, eds. H. Dejonghe, & H. J. Habing (Dordrecht: Kluwer), 209

Kuijken, K. 1996, in Barred Galaxies, eds. R. Buta, D. A. Crocker, and B. G. Elmegreen (ASP: San Francisco), 505

Kuijken, K., & Merrifield, M. R. 1995, ApJ, 443, L13

Lütticke, R., Dettmar, R.-J., & Pohlen, M. 2000a, A&AS, 145, 405

Lütticke, R., Dettmar, R.-J., & Pohlen, M. 2000b, A&A, 362, 435

MacArthur, L. A., Courteau, S., & Holtzman, J. A. 2003, ApJ, 582, 689

Mayer, L., & Wadsley, J. 2004, MNRAS, 347, 277

Merrifield, M. R. 1996, in Barred Galaxies, eds. R. Buta, D. A. Crocker, and B. G. Elmegreen (ASP: San Francisco), 179

Merrifield, M. R., & Kuijken, K. 1999, A&A, 443, L47

Mulder, W. A., & Liem, B. T. 1986, A&A, 157, 148

Navarro, J. F., Frenk, C. S., & White, S. D. M. 1996, ApJ, 462, 563

O'Neill, J. K., & Dubinski, J. 2003, MNRAS, 346, 251

Patsis, P. A., Skokos, Ch., & Athanassoula, E. 2002, MNRAS, 337, 578

Patsis, P. A., Skokos, Ch., & Athanassoula, E. 2003a, MNRAS, 342, 69

Patsis, P. A., Skokos, Ch., & Athanassoula, E. 2003b, MNRAS, 346, 1031

Peletier, R. F., & Balcells, M. 1996, AJ, 111, 2238

Peters, W. L. 1975, ApJ, 195, 617

Pfenniger, D., & Norman, C. 1990, ApJ, 363, 391

Raha, N., Sellwood, J. A., James, R. A., & Kahn, F. D. 1991, Nature, 352

Searle, L., & Zinn, R. 1978, ApJ, 225, 357

Seigar, M. S., & James, P. A. 1998, MNRAS, 299, 672

Shaw, M. A. 1987, MNRAS, 229, 691

Skokos, Ch., Patsis, P. A., & Athanassoula, E. 2002a, MNRAS, 333, 847

Skokos, Ch., Patsis, P. A., & Athanassoula, E. 2002b, MNRAS, 333, 861

Shen, J., & Sellwood, J. A. 2004, ApJ, 604, 614

Teuben, P. J. 1995, in Astronomical Data Analysis Software and Systems IV, ed. R. Shaw, H. E. Payne, & J. J. E. Hayes (ASP: San Francisco), 398

Tsikoudi, V. 1980, ApJS, 43, 365

Valenzuela, O., & Klypin, A. 2003, MNRAS, 345, 406

van den Bosch, F. C., & Emsellem, E. 1998, MNRAS, 298, 267

van der Marel, R. P., & Franx, M. 1993, ApJ, 407, 525

Wakamatsu, K.-I., & Hamabe, M. 1984, ApJS, 56, 283

Whitmore, B. C., & Bell, M. 1988, ApJ, 324, 741

Wozniak, H. 1994, A&A, 286, L5

This preprint was prepared with the AAS LaTeX macros v5.2.

Fig. 1.— Bar diagnostics as a function of viewing angle and bar strength. From left to right: no bar, weak bar, intermediate bar, and strong bar case. From top to bottom: face-view of the simulation and stellar kinematics for the bar seen end-on ($\psi = 0°$), at intermediate angle ($\psi = 45°$), and side-on ($\psi = 90°$). From top to bottom, each kinematic panel shows an edge-on view of the simulation, the extracted PVD along the major-axis, the major-axis surface brightness profile (μ_I), as well as the derived Gauss-Hermite coefficients V (mean velocity), σ (velocity dispersion), h_3 (skewness), and h_4 (kurtosis). Because of strong gradients, all grayscales are plotted on a logarithmic scale.

Fig. 2.— Fourier decompositions of the face-on density distributions as a function of bar strength (see Athanassoula & Misiriotis 2002). From left to right, the relative importance of the even Fourier terms (compared to the $m = 0$ axisymmetric term) are shown for the weakly, intermediate, and strongly barred models. The terms shown are $m = 2$ (solid line), $m = 4$ (dashed line), $m = 6$ (dot-dashed line), and $m = 8$ (dotted line).

Fig. 3.— Bar diagnostics as a function of viewing angle and time for the strong bar case. From top to bottom: the evolution of the major-axis surface brightness profile (μ_I) and the derived Gauss-Hermite coefficients V (mean velocity), σ (velocity dispersion), h_3 (skewness), and h_4 (kurtosis). From left to right: stellar kinematics for the bar seen end-on ($\psi = 0°$), at intermediate angle ($\psi = 45°$), and side-on ($\psi = 90°$). Each kinematic panel shows the time evolution of a profile in steps of 20 time units. $t = 0$ is at the bottom and the profiles are offset vertically from each other by an arbitrary amount.

Fig. 4.— Bar diagnostics as a function of viewing angle and inclination for the strong bar case. From left to right: $i = 90$, 85, 80, and 75°. From top to bottom: stellar kinematics for the bar seen end-on ($\psi = 0°$), at intermediate angle ($\psi = 45°$), and side-on ($\psi = 90°$). From top to bottom, each kinematic panel shows a properly projected view of the simulation, the extracted PVD along the major-axis, the major-axis surface brightness profile (μ_I), as well as the derived Gauss-Hermite coefficients V (mean velocity), σ (velocity dispersion), h_3 (skewness), and h_4 (kurtosis). Because of strong gradients, all grayscales are plotted on a logarithmic scale.

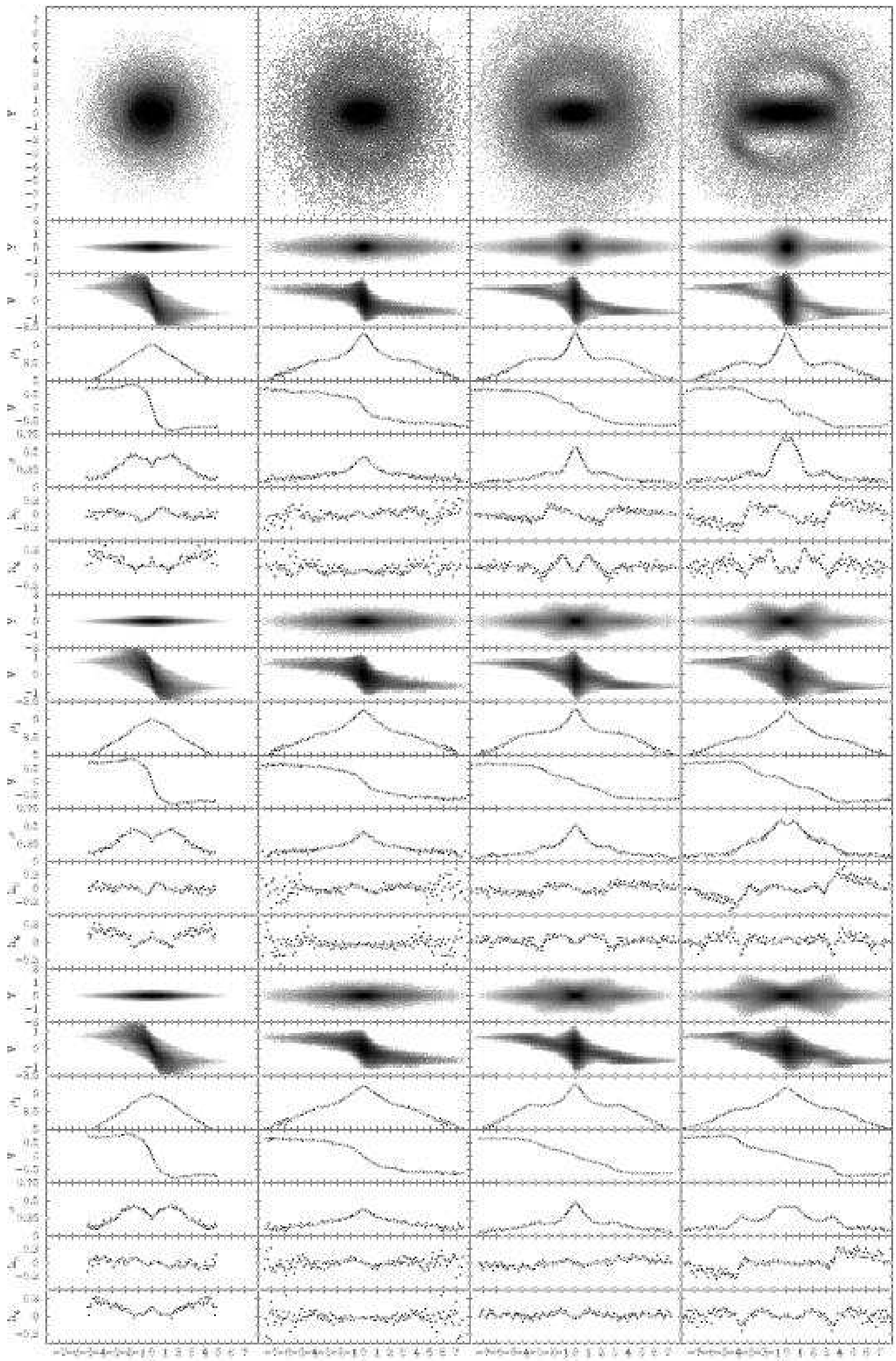

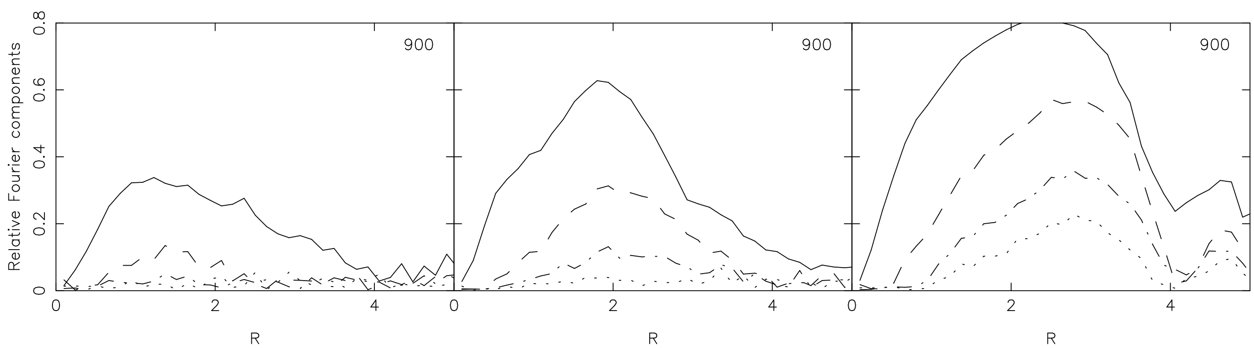

Relative Fourier components
0.8
0.6
0.4
0.2
0
900
900
900
0
2
4
R
R
R